

1 **Assimilation of snow water equivalent from AMSR2 and IMS**
2 **satellite data utilizing the local ensemble transform Kalman filter**

3
4 Joonlee lee¹, Myong-In Lee^{1*}, Sunlae Tak¹, Eunkyo Seo^{2,3}, and Yong-Keun Lee⁴

5
6 ¹ *Department of Civil, Urban, Earth, and Environmental Engineering, Ulsan National*
7 *Institute of Science and Technology, Ulsan, Korea*

8 ² *Department of Environmental Atmospheric Sciences, Pukyong National University, Busan,*
9 *South Korea.*

10 ³ *Center for Ocean-Land-Atmosphere Studies, George Mason University, Fairfax, VA, USA*

11 ⁴ *Earth System Science Interdisciplinary Center, University of Maryland, College Park,*
12 *U.S.A.*

13
14
15
16 ~~NOV 15, 2023~~

17 29 July 2024

18
19
20
21 To be submitted to GMD

23 *Corresponding author: Prof. Myong-In Lee, Department of Urban and Environmental
24 Engineering, Ulsan National Institute of Science and Technology, 50 UNIST-gil, Ulsan 44919,
25 Republic of Korea (milee@unist.ac.kr)

26 Abstract

27 Snow Water Equivalent (SWE), as one of the land initial or boundary conditions, plays a
28 crucial role in global or regional energy and water balance, thereby exerting a considerable
29 impact on seasonal and sub-seasonal scale predictions owing to its enduring memory over 1 to
30 2 months. Despite its importance, most SWE initialization remains challenging due to its
31 reliance on simple approaches based on spatially ~~constrained observation~~ limited observations.
32 Therefore, this study developed the advanced SWE data assimilation framework with satellite
33 remote-sensing data utilizing the local ensemble transform Kalman filter (LETKF) and the
34 Joint U.K. Land Environment Simulator (JULES) land model. This approach constitutes a
35 ~~novel approach that has not been previously attempted, as it offers~~ an objective ~~way to~~ method
36 that optimally ~~combine~~ combines two ~~imperfect~~ previously unattempted incomplete data
37 sources: the satellite SWE retrieval from the Advanced Microwave Scanning Radiometer 2
38 (AMSR2) and dynamically ~~balanced~~ SWE from the JULES land surface model. In this
39 framework, an algorithm is additionally considered to determine the assimilation process based
40 on the presence or absence of snow cover from the Interactive Multisensor Snow and Ice
41 Mapping System (IMS) satellite, renowned for its superior reliability.

42 The baseline model simulation from JULES without satellite data assimilation shows
43 ~~superior~~ better performance in high-latitude regions with heavy snow accumulation but
44 relatively inferior in the transition regions with less snow and high spatial and temporal
45 variation. Contrastingly, the AMSR2 satellite data exhibit better performance in the transition
46 regions but poorer in the high latitudes, presumably due to the limitation of the satellite data in
47 the penetrating depth. The data assimilation (DA) demonstrates the positive impacts by
48 reducing uncertainty in the JULES model simulations in most areas, particularly in the mid-
49 latitude transition regions. In the transition regions, the model background errors from the
50 ensemble runs are significantly larger than the observation errors, emphasizing great

51 uncertainty in the model simulations. The results of this study highlight the beneficial impact
52 of data assimilation by effectively combining both land surface model and satellite-derived
53 data according to their relative uncertainty, thereby controlling not only transitional regions but
54 also ~~satellite-constrained areas experiencing heavy snow accumulation. This assimilation~~
55 ~~framework is anticipated to contribute to a more precise prediction of atmospheric conditions~~
56 ~~by realistically capturing the interaction between the atmosphere and land, given the substantial~~
57 ~~influence of SWE on energy and water balance at the interface of the atmosphere and land~~the
58 regions with heavy snow accumulation that are difficult to detect by satellite.

59

60 **1. Introduction**

61 Snow plays a crucial role in regulating the water, energy, and carbon exchange between the
62 land surface and atmosphere (e.g., Dutra et al., 2011; Thomas et al., 2016). A snowpack tends
63 to increase surface albedo and soil moisture as the snow melts (Eagleson,1970), thereby
64 affecting the climate system through changes in water and energy balances. In addition to local
65 impacts, the continental snowpack over Eurasia can influence the large scale atmospheric
66 circulation during winter (e.g., Li and Wang, 2014) or in spring (e.g., Broxton et al., 2017).
67 Especially, the Eurasian autumn snow can affect upward-propagating stationary Rossby-wave
68 activity, leading to stratospheric warming and weakening of stratospheric polar vortex and jet
69 stream, which in turn emerges as a negative Arctic oscillation (AO)-like pattern at the surface
70 during winter due to downward propagation through the troposphere. Its impact is shown in
71 both observation and model experiments (e.g., Allen and Zender 2011; Cohen et al. 2007).
72 Furthermore, the interannual variability of snow melting during the boreal spring season affects
73 surface soil moisture in summer, which has important implications for heatwave development
74 and emphasizing mechanisms through land-atmosphere interactions (Seo et al., 2020).

75 In the subseasonal to seasonal (S2S) timescales, land initial states are crucial components
76 in the S2S timescale predictions due to the inherent memory that changes slowly for 1 to 2
77 months in the climate system (e.g., Derome et al. 2005; Chen et al., 2010; Seo et al., 2019). In
78 particular, the realistic snow initial states contribute to improving S2S prediction skills, as
79 proven in several modeling studies. For example, previous studies (Orsolini et al., 2013; Jeong
80 et al., 2013) demonstrated a considerable enhancement in prediction skill of 2m air temperature
81 up to a lead time of 1-2 months across certain regions of Eurasia and the Arctic during winter,
82 depending on snow initialization. Moreover, other studies (Orsolini et al., 2016; Li et al., 2019)
83 have revealed that wave activity propagating toward the stratosphere, influenced by snow
84 initial conditions in climate models, can induce changes in the polar vortex and contribute to

85 the persistence of the North Atlantic Oscillation (NAO) and the AO. This emphasizes the
86 significance of snow initialization in climate models as an essential process for enhancing
87 prediction performance at the S2S timescales.

88 Snow states, i.e., snow water equivalent (SWE) used directly for hydrological analysis and
89 initial states of the model (Li et al., 2019; Gan et al., 2021), are generally provided from in-situ
90 observations data, remote-sensing retrievals from satellites, or numerical models such as the
91 land surface model (LSM) operated based on the observed atmospheric variables. For the in-
92 situ data snow depth (SD) measurements prevail, largely attributed to the challenges associated
93 with acquiring precise SWE data (Takala et al., 2011; De Rosnay et al., 2014). Surface synoptic
94 observations (SYNOP) serve as the principal source for SD measurements. The in-situ
95 measurements offer the most dependable snow information, yet they are characterized by
96 relatively coarse temporal and spatial resolutions, particularly within limited areas, due to the
97 spatial heterogeneity inherent in snow distribution. (Helmert et al., 2018; Meyal et al., 2020).
98 Satellite-derived observations using conical scanning microwave instruments may provide
99 spatially consistent data coverage across the globe. Cho et al. (2017) showed the SWE retrieval
100 results from two passive microwave sensors, the advanced microwave scanning radiometer 2
101 (AMSR2) and the special sensor microwave imager sounder (SSMIS). However, the
102 algorithms for SWE retrieval exhibit a degree of sensitivity to a variety of parameters such as
103 snow liquid water content and snow grain size distribution (De Rosnay et al., 2014). Hence,
104 satellite-based SWE data still have limitations in accuracy, especially under deep snow
105 conditions due to the limited penetration depth (Gan et al., 2021). On the other hand, satellite
106 retrieval can estimate snow cover accurately under clear sky conditions (Brubaker et al., 2009).
107 Model simulations obtained from LSMs and simple snow models can cover complete
108 spatiotemporal resolution but involve potentially large uncertainties due to the deficiencies in
109 the physical parameterizations and meteorological forcing data (Dirmeyer et al., 2006; Seo et

110 al., 2021).

111 Considering that snow observation ~~datasets have their~~dataset has its respective strengths as
112 well as limitations, data assimilation or other data fusion methods can prove to be beneficial
113 for constructing snow states such as reanalysis data (e.g., Brasnett, 1999; Dee et al., 2011;
114 Meng et al., 2012; Pullen et al., 2011; De Rosnay et al., 2014). For example, the snow analysis
115 for the Canadian Meteorological Center (CMC) utilizes a 2-dimensional optimal interpolation
116 (2D-OI) scheme with in-situ observations and the outputs from a simple snow model (Brown
117 et al., 2003). The National Centers for Environmental Prediction (NCEP) climate forecast
118 system reanalysis (CFSR) combines a multi-satellite-based interactive multi-sensor snow and
119 ice mapping system (IMS) as satellite-based snow cover retrieval and the outputs from the
120 global snow model of the Air Force Weather Agency (Meng et al., 2012). At the European
121 Center for Medium Weather Forecast (ECMWF), the ECMWF reanalysis (ERA)-Interim and
122 ERA5 for the snow analysis employ a Cressman interpolation and 2D-OI, respectively, with
123 the IMS, in-situ observation, and the results from a land surface model (Dee et al. 2011; De
124 Rosnay et al., 2014). The Japanese 55-year Reanalysis (JRA55) also utilizes the 2D-OI with
125 in-situ observation, satellite-based snow cover from SSMIS, and the results from an LSM
126 (Kobayashi et al., 2015). Given that the majority of the reanalysis datasets rely on snow depth
127 measurements, the SWE estimation is likely to introduce potential accuracy concerns when the
128 snow depth information is combined with the snow density calculations.

129 Climate prediction systems in operational centers such as the Meteorological Office (Met
130 Office) in the United Kingdom and the Korean Meteorological Administration (KMA) conduct
131 the snow initialization by utilizing the results of the operational global unified model (UM) and
132 the IMS snow cover, which solely indicates the presence of snow (Pullen et al., 2011), lacking
133 in its ability to reflect the physical quantity of it. The initialization at NCEP also performs a
134 similar approach using input data combined from IMS snow cover and results from the global

135 SD model (SNODEP; Meng et al., 2012). Furthermore, the snow initialization of ECMWF
136 employs optimal interpolation with a combination of results from the LSM, IMS snow cover,
137 and in-situ observation from SYNOP and national networks available on the GTS. However,
138 in regions where ground observations are unavailable, large errors may exist in the snow model
139 outputs due to uncertainties in atmospheric forcing and imperfect model parameterization
140 (Boone et al., 2004; Essery et al., 2009). Often, the snow processes parameterized in LSMs
141 rely on observed properties sampled in limited areas (Lim et al., 2022). In addition, as IMS
142 snow cover only identifies the presence of snow, the data assimilation with the satellite snow
143 cover only is not sufficient and inappropriate in constraining water and energy conservation.
144 Alternative methods that consider the physical quantity of snow are required for the snow
145 initialization.

146 One approach to mitigate the spatial discontinuity of ground observations is to use satellite-
147 derived SWE with wide spatial coverage and frequent temporal resolution. However, the SWE
148 retrievals from satellites still have considerable uncertainties (De Lannoy et al., 2010; Dawson
149 et al., 2018), which can arise from vegetation and terrain interference, sensor signal saturation,
150 snowfall amount, and simplifications in the underlying assumptions of the retrieval algorithms
151 (Liu et al., 2015). In particular, a region with heavy snow accumulation leads to a significant
152 underestimation of SWE due to the limitations in penetration depth from satellites (Gan et al.,
153 2021), so that satellite-derived SWE is not employed in the land initialization process. In
154 previous studies, various approaches have been attempted to improve SWE product
155 performance, such as combining satellite-derived SWE with ground observations (Pulliainen
156 et al., 2020), different satellite data sets (Gan et al., 2021), simple snow models (Dziubanski
157 and Franz, 2016), or LSMs (Kwon et al., 2017; Kumar et al., 2019). However, most previous
158 studies have focused on targeted regions with limited ground-based observations. Snow
159 initialization in global coverage using satellite-derived SWE remains a persistently challenging

160 task.

161 Therefore, this study developed an advanced SWE data assimilation framework with satellite
162 remote-sensing data using the local ensemble transform Kalman filter (LETKF) and the Joint
163 U.K. Land Environment Simulator (JULES) land model. ~~This constitutes a novel approach that
164 has not been previously attempted, and it offers an objective way to optimally combine two
165 imperfect~~While there are existing studies on SWE data assimilation (e.g., Oaida et al., 2019;
166 Smyth et al., 2020; Luoju et al., 2021), the use of passive microwave observations based on
167 the LETKF in this context is relatively rare (e.g., Giroto et al., 2020). This approach constitutes
168 an objective method that optimally combines two previously unattempted incomplete data
169 sources: the satellite SWE from the Advanced Microwave Scanning Radiometer 2 (AMSR2)
170 and the dynamically-balanced SWE from the JULES land model forced by observed
171 atmospheric fields. The estimated SWE data exhibit better consistence by additionally using
172 snow cover data from the IMS data. This assimilation framework also enables the assessment
173 of improvement as it provides insights into the reasons behind the performance improvement
174 based on the Kalman gain analysis that measures the relative significance of the input data
175 between the satellite and the land model during the data assimilation cycle. The satellite data
176 have demonstrated high reliability in the transition regions of climatologically-shallow snow
177 conditions (Gan et al., 2021), and these regions are known as "hot spots" of strong atmosphere-
178 land coupling through snow melting and associated surface energy and water balance changes
179 (Koster et al., 2004; Dirmeyer, 2011; Huning and AghaKouchak, 2020). From these
180 perspectives, it would be important to evaluate the impact of satellites on the transition regions
181 as well as on the deep accumulation regions where accurate satellite retrievals are challenging.
182 Furthermore, the benefits of assimilating satellite retrievals in extremely high-temperature
183 events, such as the case in April 2020 over Eurasia, can be elucidated. In this regard, we expect
184 that this snow data assimilation framework with satellite-derived SWE can be significant in

185 providing optimal snow initial states for improving the S2S prediction by global climate models.

186

187 **2. Data and model**

188 **2.1. Satellite data**

189 The snow information including snow cover and SWE can be derived from satellite
190 measurements offering global coverage and high temporal as well as spatial resolution. For
191 data assimilation, this study uses SWE calculated from brightness temperature measurements
192 obtained by the AMSR2 on board the Japanese Aerospace Exploration Agency (JAXA) global
193 change observation mission-water (GCOM-W) satellite. This AMSR2 Unified Level-3 (L3)
194 dataset offers daily estimation of SWE at 25 km resolutions from July 2012 to the present.
195 AMSR2 has a sensor designed to detect microwave radiation naturally emitted from the surface
196 and atmosphere, employing six frequency bands ranging from 6.9 to 89 GHz. Through this
197 conical scanning mechanism, AMSR2 can acquire day and night datasets with nearly constant
198 spatial resolution over more than 99% of the global coverage every two days. Comprehensive
199 explanations of AMSR2 characteristics are available in Imaoka et al. (2010). AMSR2 is
200 selected for the assimilation because it produces more accurate results by assimilating data
201 from modern sensors (e.g., AMSR2) compared to data from conventional sensors (e.g., AMSR-
202 E) (Cho et al., 2017).

203 The widely used multisensor-derived snow cover is IMS (e.g., Ramsay 1998; Helfrich et
204 al., 2007) produced by NOAA the National Environmental Satellite Data and Information
205 Service (NESDIS) for the Northern Hemisphere from February 2004 to the present at 4 km
206 resolutions. This dataset is generated using various data products, including multi-satellite
207 images and in-situ observations (U.S. National Ice Center, 2008). Since IMS provides binary
208 (0: no snow or 1: snow covered) snow cover information, we transform the IMS snow cover at
209 4 km grids to the snow cover fraction (SCF) within a 50-km LSM grid by counting the snow
210 pixel number with a value of 1. A 50-km LSM grid is declared as snow-covered when more
211 than 50% of the 4km pixels within the grid are covered with snow. In this study, the application

212 of the assimilation process is determined based on IMS-based SCF, renowned for its superior
213 reliability (e.g., Brown et al., 2014). Further details will be described in Section 3.3.

214

215 **2.2. Reference data for SWE and SCF**

216 The CMC daily estimated SWE is used for verification. The SWE data is processed using
217 statistical interpolation between a background field derived from a simple snow model and in-
218 situ daily SD (Brown and Brasnett, 2010). In detail, this dataset utilizes optimal interpolation
219 methods to acquire spatial SD from the in-situ data, involving SYNOP, special aviation reports
220 from the World Meteorological Organization (WMO), and meteorological aviation reports
221 (METAR). In areas with scant in-situ data, a simple snow accumulation and melt model is
222 employed to create an optimal interpolation that estimates snowmelt and snowfall worldwide,
223 assuming the persistence of the snowpack mass between snowfall and melting events
224 (Brasnett, 1999). Although the average elevation of snow measurement stations used in CMC
225 is biased toward low elevations ($< 400\text{m}$), potentially causing relative negative biases at higher
226 elevations with heavy snow accumulation, the CMC dataset is often considered the premier
227 snow analysis accessible in the Northern Hemisphere (Su et al. 2010) and has still been widely
228 used to evaluate model outputs (e.g., Reichle et al., 2011; Reichle et al., 2017; Toure et al,
229 2018). Therefore, the SWE of CMC produced without the satellite-derived data is selected for
230 verification as an independent dataset for evaluating the assimilated analysis with remote
231 sensing snow retrievals. Since only daily SD analysis is provided in CMC, it is converted to
232 daily SWE based on the snow bulk density methods (e.g., Sturm et al., 2010). It is available
233 from 12 March 1998 to the present and offers comprehensive coverage of the entire Northern
234 Hemisphere with a horizontal resolution of 24 km. The SWE of CMC at its native horizontal
235 resolution is interpolated onto the LSM grid through local area averaging.

236

237 **2.3. JULES LSM**

238 This study utilizes the JULES LSM from the Met Office (Best et al., 2011), a component
239 land model of the global seasonal forecasting system version 6 (GloSea6) global, fully-coupled
240 atmosphere, ocean, land, and sea-ice model. The surface types (or snow tiles) in the JULES
241 LSM consist of four non-vegetated types: urban, land-ice, inland water, and bare soil, as well
242 as five vegetation functional types: C3 temperate grass, needleleaf trees, shrubs, C4 tropical
243 grass, and broadleaf trees. For each surface tile, a separate energy balance is computed, and the
244 average energy balance in the grid cells is determined by applying weights to the values of each
245 surface tile. Two schemes are used within JULES to represent surface snow (e.g., Best et al.,
246 2011; Burke et al., 2013). The simple method involves a zero-layer approach, which modifies
247 the top soil level without using explicit model layers to represent snow processes. The other is
248 the multi-layer approach which is more comprehensive, described in Best et al. (2011). In the
249 case of vegetated surfaces, snow can be separated into ground snow and canopy snow or stored
250 in a single effective reservoir. As both the zero-layer and multi-layer snow models provide
251 similar results under various conditions (Best et al., 2011), this study used the zero-layer snow
252 model with constant thermal conductivity and density for snow. Although the heat capacity of
253 snow is ignored, the bulk thermal conductivity in the surface layer is reduced as the thermal
254 conductivity of snow differs from that of the soil and the layer thickness increases. As long as
255 snow persists on the ground, the skin temperature cannot exceed 0°C, yet the heat flux utilized
256 for melting the snow is diagnosed as the residual in the surface energy balance. The melted
257 water is immediately drained from the snow, divided into runoff and soil infiltration, and liquid
258 water is not stored or frozen in the snow. A detailed description of the energy and water cycling
259 in the JULES LSM can be referenced in Best et al. (2011).

260 The prognostic variables (e.g., SWE) in the LSM are determined by meteorological forcing
261 variables such as 2-m air temperature, humidity, 10-m wind speed, precipitation, surface

262 pressure, and radiative fluxes. The 3-hourly, JRA55 reanalysis at 0.56° spatial resolution is
263 employed for the meteorological forcing variables, which is linearly interpolated to a 50 km
264 resolution of the LSM. The model background error needed for data assimilation is estimated
265 by JULES ensemble runs with perturbed initial and boundary conditions. Following the
266 previous studies (Reichle et al., 2008; Seo et al., 2021), meteorological forcing variables are
267 perturbed to account for the uncertainties in these variables, especially precipitation, downward
268 shortwave, and downward longwave. Perturbations are applied using additive adjustments
269 assuming a normal distribution for longwave radiation and multiplicative adjustments
270 following a log-normal distribution for shortwave radiation and precipitation, as guided by
271 previous studies (Seo et al., 2021). Here, the ensemble means of additional and multiplicative
272 perturbations are zero and one, respectively. The relationship between disturbed precipitation
273 and radiative flux ensures the physical consistency among atmospheric forcing variables
274 (Reichle et al., 2008). For instance, a negative anomaly in precipitation and downward
275 longwave-radiation is statistically linked to a positive anomaly of downward shortwave-
276 radiation. Detailed explanations regarding the perturbation of atmospheric forcings can be
277 found in Reichle et al. (2008).

278

279 **3. Methodology**

280 **3.1. Bias correction**

281 The discrepancy in SWE between remote sensing and LSMs often arises due to uncertainties
282 in the model physics and forcing data and satellite retrievals. These uncertainties can lead to a
283 significant discrepancy in SWE between model simulations and satellite remote-sensing
284 retrievals, potentially degrading performance. In previous studies (e.g., Reichle and Koster,
285 2004; Seo et al., 2021), a scaling method of the nonlinear cumulative distribution function
286 (CDF) matching is used to account for the systematic bias of soil moisture in the model
287 backgrounds. However, unlike soil moisture, SWE presents varying characteristics in the CDF
288 distribution across different regions, such as between high and low latitudes, thus requiring the
289 estimation of distribution at each grid point. As a result, the insufficient sample size hinders
290 the clear simulation of the CDF distribution, posing challenges in its application. To address
291 this issue, we attempted to apply a simple and effective standard normal deviation scaling to
292 satellite-derived SWE at each grid point, considering its potential use as initial conditions for
293 JULES LSM-based climate models. Based on the climatology and standard deviation for the
294 model and remote sensing retrievals, the scaled SWE (O_{new}) from the satellite can be derived
295 from the following relation:

296

$$297 \quad O_{new} = \left(\frac{O - \bar{O}}{\sigma_o} \times \sigma_m \right) + \bar{M} \quad (1)$$

298

299 where $\bar{O}(\sigma_o)$ and $\bar{M}(\sigma_m)$ indicate climatology (standard deviation) of remote sensing
300 retrievals and the model, respectively. This approach has been widely utilized in observation-
301 based land initialization and has proven to be effective (e.g., Koster et al., 2011; Jeong et al.,
302 2013).

303

304 **3.2. Data assimilation method**

305 The snow assimilation is conducted based on the LETKF (e.g., Hunt et al., 2007), which is
306 utilized to combine remotely sensed retrievals with the LSM model outputs (a.k.a. backgrounds)
307 at each grid point to produce a snow analysis. Unlike variational data assimilation methods,
308 non-variational approaches (i.e., ensemble-based filters) characterize a probabilistic
309 representation with the spread of the ensemble serving as an estimate of forecast uncertainty.
310 LETKF has several advantages over other data assimilation methods. First, LETKF can
311 efficiently handle large datasets and high-dimensional state variables by localizing the
312 covariance matrix. This offers efficiency in parallel computing, making it suitable for real-time
313 forecasting and high-resolution data assimilation. In this study, the horizontal local patch size
314 and the localization length scale parameters are defined as 150 km and 30 km (Table 1),
315 respectively. This approach involves the weight function for the covariance localization within
316 the local patch centered at the analysis grid (e.g., Houtekamer and Mitchell, 2001; Hamill et
317 al., 2001). This function assigns larger errors to observations located farther away from the
318 center of the local patch, as proposed by Miyoshi and Yamane (2007), depending on the
319 Gaussian function. Secondly, the method utilizes model simulation ensembles to capture the
320 uncertainty in the initial states and background errors, which allows for a better representation
321 of the flow-dependent probability distribution of the state variables that vary in time and space.
322 Third, the LETKF employs an inflation parameter to adjust the ensemble spread, ensuring
323 realistic uncertainty estimation by accounting for background errors. The underestimation of
324 the analysis error covariance is typically issued by spatially and temporally constant boundary
325 conditions and observation errors and limited ensemble members. Based on the standardized
326 LETKF, this study applies a multiplicative covariance inflation of 20% of the spread of 24
327 member ensembles for each data assimilation cycle. Furthermore, the Kalman gain analysis
328 (Seo et al., 2021), which quantifies the ratio of the background error to the total error

329 (equivalent to the sum of the background and the observation error), is conducted. This analysis
330 serves to determine the weights assigned to assimilated observations in the analysis update
331 processes of the LETKF.

332

333 3.3. Snow data assimilation design

334 This study conducts the advanced daily cycle snow data assimilation experiment at ~~a daily~~
335 ~~cycle based on each grid point using the~~ LETKF ~~with~~based on the satellite data and the JULES
336 LSM model outputs driven by 3-hourly JRA55 reanalysis atmospheric forcing. The snow
337 assimilation processes are illustrated in Fig. 1, with a more detailed description in Table 1.
338 Since data assimilation is conducted by considering the error of SWE in both the model and
339 the observation, it is important to accurately understand the observation and background errors
340 to improve the performance of data assimilation. The experiment calculates the background
341 error from the 24 ensemble member spreads generated by perturbing atmospheric forcings such
342 as longwave radiation, shortwave radiation, and precipitation in JULES LSM, as provided in
343 section 2.3. Due to the absence of precise error estimates for AMSR2 SWE retrievals, the
344 observation error is conservatively prescribed as 10% of AMSR2 SWE for each grid compared
345 to the previous study utilizing AMSR2 SWE data (Lee et al., 2015), considering the general
346 increase in the errors during the snow accumulation period with the development of deep
347 snowpack (Foster et al., 2005; Cho et al., 2017). Here, the bias-corrected AMSR2 satellite data
348 as described in section 3.1 is used as the observation data, and the updated snow analysis state
349 through data assimilation becomes a new initial state for the next integration in JULES LSM
350 (Fig. 1). In addition, the analysis state of this method is calculated based on the IMS snow
351 cover fraction as ~~a reference in the following way follows~~ (Fig. 1); ~~where~~. ~~If~~ the SCF ~~off~~from
352 IMS is ~~zero~~0, the snow ~~amount~~ analysis is set to zero, ~~and in other cases; otherwise~~, it is derived
353 ~~from~~through data assimilation. The reason for this is due to the importance of the presence or

354 absence of snow in the climate system, as well as the high reliability of the IMS data (e.g.,
355 Brown et al., 2014). A background experiment of JULES LSM without satellite data
356 assimilation as a baseline (referred to hereafter as “Openloop”) is also achieved by employing
357 the same ensemble perturbations, thereby measuring the skill improvement from the snow
358 analysis state through the assimilation of satellite-derived SWE and IMS SCF from satellite
359 and surface observations (referred to hereafter as “DA”). All experiments are conducted in
360 April from 2013 to 2020, which is one of the months with low snow performance in the LSM
361 when the snow begins to melt in the Northern Hemisphere (e.g., Toure et al., 2018; You et al.,
362 2020).

363 4. Results

364 4.1. Skill Verification

365 Figure 2 displays the climatological-mean SCF from the IMS multi-satellite data (Brown
366 et al., 2014) and the differences from AMSR2, Openloop, JRA55, and DA for April 2013-2020.
367 Here, the JRA55 SWE serves as a reference dataset for comparison with other reanalyses and
368 is associated with meteorological forcing data used in the JULES land surface model. April is
369 a season when the accumulated snow during the cold season begins to melt. This study defines
370 the transitional region with a climatological-mean SWE of less than 16 mm as in previous
371 studies (e.g., Gan et al., 2021), the boundary of these transition regions is represented by the
372 black lines in Fig. 2. The transitional regions exhibit large variability in space and time, and
373 they are mainly located at mid-latitudes. The SCF climatology patterns show negligible
374 differences in high latitudes of heavy snow accumulation but noticeable differences in the
375 transitional mid-latitude regions of less snow. SCF from JRA55 tends to be underestimated
376 compared to IMS, whereas AMSR2 and Openloop tend to overestimate. There is a clear
377 difference in SCF between AMSR2 and IMS satellite data. This study gives more credibility
378 to IMS than AMSR2, as the former is based on multiple satellite data sources (e.g., Brown et
379 al., 2014). As we used the IMS SCF to define the snow region to be assimilated by AMSR2
380 SWE, it is natural that DA shows better consistency with IMS and reduces overestimation
381 biases in Openloop. Quantitatively, the root mean square differences (accuracy, defined in
382 supplementary Table 1 as in previous study) for AMSR2, Openloop, JRA55, and DA with
383 (from) IMS are 0.23 (0.91), 0.18 (0.91), 0.13 (0.93), and 0.13 (0.97), respectively, showing the
384 best consistency in DA. The quantitative differences between DA and other experimental
385 results are minor, but noticeable spatial discrepancies exist, particularly around transition
386 regions.

387 The SWE climatology from AMSR2, Openloop, JRA55, and DA is also compared with

388 CMC as a reference in Fig. 3. The SWE derived from AMSR2 shows a significant
389 underestimation compared to CMC, particularly in the regions with heavy snow accumulation
390 at high latitudes. This is presumed to be due to limitations in satellite sensors detecting the
391 depth of snow (Gan et al., 2021). The SWE from JRA55 exhibits characteristics of
392 overestimation in high latitudes and underestimation in transitional regions. On the other hand,
393 the climatological SWEs from Openloop and DA exhibit higher correspondence to CMC, even
394 higher than JRA55. Specifically, DA demonstrates a higher agreement with CMC, despite the
395 marginal difference compared to Openloop. Quantitatively, the pattern correlation coefficients
396 (root mean square differences) for AMSR2, Openloop, JRA55, and DA with (from) CMC are
397 0.63 (80.7 kg/m²), 0.80 (50.1 kg/m²), 0.60 (100.8 kg/m²), and 0.80 (49.9 kg/m²), respectively.
398 Due to the application of standard deviation scaling to the satellite-derived SWE used in data
399 assimilation, the discrepancy in climatological SWE distributions between DA and Openloop
400 is deemed negligible. Despite its similarity to Openloop, DA with snow data assimilation
401 displays the relatively highest correlation and the smallest root mean square difference among
402 the datasets.

403 Next, we compare the temporal variation of SWE as measured by the Spearman rank
404 correlation coefficient with CMC, which is regarded as more appropriate than the Pearson
405 correlation coefficient for describing datasets containing nonlinearity and outliers such as snow
406 in both time and space. Figure 4 compares the distribution of correlation skills from AMSR2,
407 Openloop, JRA55, and DA. Openloop has a high performance in regions with heavy snow
408 accumulation but relatively low performance in transition regions with significant snow
409 changes. In contrast, the results from the AMSR2 satellite data represent poor performance in
410 high-latitude areas with heavy snow accumulation but high performance in transitional regions,
411 consistent with the previous studies (Gan et al., 2021). DA shows high performance not only
412 in high-latitude areas with heavy snow accumulation but also in transition regions. Even

413 compared to JRA55 used as the atmospheric forcing, DA performs better in temporal variation.
414 The quantitative results in the correlation in the Northern Hemisphere over 40°N (the transition
415 region) are 0.41 (0.54) for AMSR2, 0.61 (0.48) for Openloop, 0.58 (0.58) for JRA55, and 0.67
416 (0.61) for DA, respectively. The findings indicate that satellite retrievals offer additional value
417 in capturing temporal variations through data assimilation, indicating the benefit of
418 assimilating the AMSR2 SWE despite the overall lower performance of the satellite data itself.

419 The performance improvement by DA is also evident in the zonally-averaged correlation
420 coefficient shown in Fig. 5. The AMSR2 satellite data shows higher performance than
421 Openloop in the transition region around latitude 45 °N-55 °N, although performance sharply
422 decreases with increasing snow accumulation. Openloop indicates gradually increasing
423 performance as the latitude increases, with the highest performance at around 60°N. DA
424 denotes superior performance across the Northern Hemisphere, especially in the mid-latitude
425 transition region than AMSR2 or JRA55. An exception is for 35-40°N in the Tibetan Plateau,
426 where JRA55 used in-situ observations. The results suggest that the developed snow data
427 assimilation system represents well not only the transitional regions but also the ~~satellite-~~
428 ~~limited~~ regions with heavy/high snow accumulation that are difficult to detect by satellite.

429 Figure 6 presents the Spearman rank correlation depending on the SWE amount in the
430 Northern Hemisphere. AMSR2 exhibits higher performance than Openloop for SWE up to 16
431 mm. However, the performance of AMSR2 sharply declines beyond that threshold, and
432 Openloop shows a better performance. Consistent with the results illustrated in Figs. 4 and 5,
433 DA demonstrates superior performance compared to others. Note that DA performs
434 significantly better in the transition region of less than 16 mm of SWE. Considering that the
435 area below 16 mm of SWE accounts for approximately 53% of the entire area of the Northern
436 Hemisphere(as shown in the pie chart in Fig. 6), the data assimilation impact is identifiable,
437 and it can contribute substantially to the increase in the prediction skill through improving the

438 simulation of the albedo changes and surface energy balance.

439 Consistent with the description in Section 3.3, this study considers an algorithm based on
440 the highly reliable IMS satellite SCF data to identify the presence of snow and determine the
441 assimilation process. Therefore, a further sensitivity test is conducted to investigate the
442 influence of incorporating IMS data in snow assimilation. Figure 7 compares the correlation
443 differences between Openloop and the data assimilation result employing both AMSR2 and
444 IMS (DA), as well as the data assimilation result utilizing solely AMSR2 and excluding IMS
445 (hereafter referred to as DA_AMSR2). The results obtained from the snow assimilation show
446 the improvements in the transitional regions where AMSR2 denotes a better agreement with
447 the observations compared to Openloop. Notably, the skill is enhanced significantly in DA by
448 incorporating the IMS SCF. DA exhibits inferior performance compared to Openloop in certain
449 exceptional cases, which may be attributed to discrepancies in snow identification between the
450 CMC observations used for correlation and the IMS data utilized for data assimilation.
451 Moreover, the performance of SWE improves even when only AMSR2 is used, but
452 incorporating IMS leads to a substantial improvement in the transitional regions. This implies
453 that IMS has a positive influence on the snow data assimilation.

454

455 **4.2 Kalman gain analysis**

456 In order to better understand the skill enhancement through snow assimilation of satellite
457 data, this section examines the Kalman gain. Figure 8 illustrates the spatial distribution of
458 observation error, model background error, and the Kalman gain for SWE. A high value of the
459 Kalman gain denotes that the assimilated result is closer to the AMSR2 observation than the
460 model background. The Kalman gain is large when the background error becomes large, or the
461 observation error is small. As this study specifies the observation error as a conservative 10%
462 of SWE compared to the previous study (Lee et al., 2015), the observation error basically

463 follows the distribution similar to the climatological-mean values. The background errors,
464 originating from the 24 ensemble members, have higher values in high-latitude regions and
465 mid-latitude regions. Data assimilation methods such as LETKF used in this study often face
466 challenges in accurately representing background errors when the ensemble spread is
467 insufficient. Generally, the magnitude of ensemble spread is frequently compared to the root
468 mean square error (RMSE). The ensemble spread in this study demonstrates a sufficiently valid
469 magnitude in comparison with the RMSE, as illustrated in SFig. 1, indicating that it is well
470 estimated. Moreover, the SWE standardized distribution of SWE among the ensemble members
471 ~~consistently exhibited~~ exhibits a quasi-Gaussian distribution centered around zero, with the
472 transition region showing a ~~distinct~~ this closer resemblance to a standardized Gaussian
473 distribution particularly evident in transitional regions (SFig. 4). In the spatial distribution of
474 Kalman gain in Fig. 8c, significant performance improvement is observed in transition regions,
475 where Kalman gains exhibit larger values. However, in high-latitude areas with substantial
476 snow accumulation, there is a tendency for Kalman gain to have lower values. These findings
477 agree well with the bar graph in Fig. 9, which illustrates the Kalman gain as a function of SWE
478 amount. In the region encompassing the transition region with SWE amounts below 20 mm,
479 the Kalman gain displays the highest values, particularly exceeding 0.8. As the SWE amount
480 increases, the Kalman gain decreases, with a significant decline observed when the SWE
481 amount reaches 80-100 mm or higher. Furthermore, in the areas where DA denotes improved
482 skill compared to Openloop, the Kalman gain shows values generally above 0.7. In contrast,
483 relatively lower values below 0.5 are observed in the areas with decreased skill. This indicates
484 that in the dominant areas of performance improvement, including the transition region, the
485 background error is significantly larger than the observation error, emphasizing the substantial
486 influence of observations in data assimilation. It is found that accurate remote sensing retrievals
487 are well reflected in regions with high uncertainty in the LSM through the snow data

488 assimilation system, leading to performance improvement.

489 **4.3 Validation of the SWE for the extreme event**

490 In April 2020, Siberia experienced a record-breaking heatwave with the highest observed
491 average temperature. This section investigates the potential benefits of snow assimilation using
492 satellite data for the case of the 2020 Siberian heatwave. Previous studies have identified the
493 strong polar vortex accompanied by the AO amplification during winter as a major cause of
494 the cold Eurasian region (Overland and Wang, 2021). Additionally, it has been revealed that
495 the occurrence of high temperatures in the Siberian region is found to be closely associated
496 with large-scale atmospheric waves in the upper atmosphere over the Eurasian region
497 originating from the Atlantic (De Angelis et al., 2023). As a result, remarkable snow melting
498 occurred due to the high surface temperature over the Siberian region in April 2020, leading to
499 extremely low values of SWE and SCF as depicted in SFig. 2. This is consistent with previous
500 studies reporting a significant snow depletion in 2020 in the region (Gloege et al., 2022).
501 Especially, as shown in Fig. 10, significant negative anomalies in SWE and SCF are
502 predominant over the transition region. Substantial snow melt can contribute to record-
503 breaking heatwaves through albedo feedback and changes in the ratio of the latent and sensible
504 heat fluxes from the exposed surface, coupled with favorable atmospheric circulation patterns
505 (Collow et al., 2022). Collow et al. (2022) demonstrated that the exposed surface contributed
506 to up to 20% of the temperature anomaly over Siberia in spring 2020. This implies the
507 importance of realistic snow initial states in the global coupled model forecasts. For the
508 Siberian region with extreme high-temperature events marked by the red box in Fig. 10, DA
509 shows a better agreement with the extremely dry snow conditions, especially in the transitional
510 region, compared to the Openloop. These results are evident when considering the observation-
511 to-model ratio in that region. The percentage of CMC (IMS) is 83% (78%) for Openloop and
512 93% (89%) for DA, indicating that DA with snow data assimilation based on satellite data

513 effectively replicates the observed snow depletion in comparison with Openloop. Similarly to
514 the 2020 case, we obtained another significant case in 2014 compared to Openloop, as shown
515 in SFig. 3. Such extremely dry snow conditions can provide significant heatwave events in the
516 following months.

517

518

519

520

521

522

523 **5. Conclusions and discussion**

524 The advanced SWE data assimilation is developed in this study with the LETKF data
525 assimilation method and the JULES LSM. The system assimilates snow water equivalent
526 retrievals from AMSR2 and IMS snow cover. This constitutes an objective way to optimally
527 combine two imperfect data sources for SWE from satellite remote sensing data and the land
528 surface model simulation forced by observed atmospheric data. This study shows that the
529 satellite-derived SWE has limitations in penetrating deep snow and exhibited much
530 discrepancy from the SWE obtained from the Openloop LSM simulations. The SWE
531 assimilation in this study proves the beneficial impacts of using satellite snow data, maintaining
532 better analysis quality by dynamically balancing the errors from the satellite observations and
533 the model background states.

534 It is found that the simulation from Openloop as a baseline shows superior performance in
535 high-latitude regions with heavy snow accumulation but relatively inferior performance in
536 transition regions with much variation of snow in space and time. Contrastingly, the AMSR2
537 satellite data represent poor performance in high-latitude regions but exhibit relatively better
538 performance in the transition regions. The SWE from the LETKF data assimilation consistently
539 exhibits better performance in capturing the climatology and temporal variation compared to
540 other results. It specifically improves the analysis in the mid-latitude transition regions that
541 cover approximately 53% of the entire areas of the Northern Hemisphere. It is found that the
542 model background errors estimated from the ensemble spread are significantly larger than the
543 observation errors, thereby reflecting satellite information more in those regions. The LETKF
544 data assimilation also proves reliable representation in the heavy snow regions due to low
545 ensemble spread and large uncertainty in the satellite retrievals. Moreover, during the record-
546 breaking heatwave in Siberia in April 2020, the remarkable snow depletion observed due to
547 high surface temperatures is more realistically reproduced by our snow analysis compared to

548 the Openloop.

549 This snow data assimilation framework is anticipated to contribute to a more precise
550 prediction of atmospheric conditions by realistically capturing the interaction between the
551 atmosphere and land, given the substantial influence of SWE on energy and water balance at
552 the interface of the atmosphere and land. Specifically, this applies to the transitional regions
553 with high spatial and temporal variability. The long-term analysis of snow manifests a
554 pronounced variability in the continental interior at the interannual timescales, potentially
555 improving the prediction of extreme heatwave events by global climate models. This study
556 used the gridded CMC data from in-situ observations for the validation. Although existing
557 snow data are subject to much uncertainty and limitations, we expect to obtain comparable
558 conclusions and significant benefits of optimally combining satellite SWE data and the LSM
559 model simulations through LETKF data assimilation method.

560 The quality of the observation is crucial in the data assimilation system. Satellite-derived
561 snow cover exhibits a significantly higher accuracy compared to other data sources, while SWE
562 has restricted performance due to the limitations of penetration depth by satellite sensors and
563 relies heavily on estimation algorithms. Due to these problems, most previous studies and
564 operational centers primarily depend on satellite-derived snow cover for snow initialization.
565 However, the findings from this study highlighted the beneficial impacts of using satellite-
566 derived SWE, particularly in the rapidly changing transition areas, to find out which variable
567 is more important in closing surface energy and water balance changed by snow. Nevertheless,
568 areas of significance in large-scale circulation, such as the Tibetan region, which experiences
569 significant uncertainty and degraded performance in satellite data, do not exhibit substantial
570 data assimilation effects. As the performance of SWE derived from various satellites continues
571 to advance, these issues will be discussed more.

572

573 **Key words**

574 Snow data assimilation, AMSR2, LETKF, snow water equivalent, JULES LSM

575

576 ***Data availability.***

577 The AMSR2 SWE and IMS SC were obtained from
578 https://n5eil01u.ecs.nsidc.org/AMSA/AU_DySno.001/ and
579 <https://noadata.apps.nsidc.org/NOAA/G02156/>, respectively. The CMC SWE was collected
580 from https://daacdata.apps.nsidc.org/pub/DATASETS/nsidc0447_CMC_snow_depth_v01/.

581 The snow-assimilated results and land surface variables from the LSM offline simulation may
582 be requested from the authors.

583

584 ***Author contributions.***

585 LJI conceived the project, designed the study, developed the snow assimilation system, wrote
586 the paper, and made the figures. LMI provided advice on the methods, project design, and
587 review and editing of the manuscript. TSL helped with the experiment with the land surface
588 model. SEK helped with the data assimilation method based on LETKF. LYK provided advice
589 on snow satellite data and the sensitivity methods. All authors contributed to the writing of the
590 paper by providing comments and feedback.

591

592 ***Competing interests.***

593 The contact author has declared that none of the authors has any competing interests.

594

595 *Acknowledgements*

596 This work was funded by the Korea Meteorological Administration Research and Development
597 Program under Grant KMI2021-01210. ES was supported by Learning & Academic research
598 institution for Master's·PhD students, and Postdocs (LAMP) Program of the National Research
599 Foundation of Korea (NRF) grant funded by the Ministry of Education (RS-2023-000301702).

600

601

602

603 **Reference**

- 604 Allen, R.J., Zender, C.S.: Forcing of the Arctic Oscillation by Eurasian snow cover. *J. Clim.* 24 (24),
605 6528–6539, 2011.
- 606 Best, M.J., Pryor, M., Clark, D.B., Rooney, G.G., Essery, R., Ménard, C.B., Edwards, J.M., Hendry, M.A.,
607 Porson, A., Gedney, N., Mercado, L.M., Sitch, S., Blyth, E., Boucher, O., Cox, P.M.,
608 Grimmond, C.S.B., Harding, R.J.: The Joint UK Land Environment Simulator (JULES), model
609 description–Part 1: energy and water fluxes. *Geosci. Model Dev.* 4, 677–699, 2011.
- 610 Boone, A., Habets, F., Noilhan, J., Clark, D., Dirmeyer, P., Fox, S., Gusev, Y., Haddeland, I., Koster, R.,
611 Lohmann, D., Mahanama, S., Mitchell, K., Nasonova, O., Niu, G.Y., Pitman, A., Polcher, J.,
612 Shmakin, A., Tanaka, K., van den Hurk, B., Verant, S., Verseghy, D., Viterbo, P., Yang, Z.L.: The
613 Rhone-Aggregation land surface scheme intercomparison project: an overview. *J. Clim.* 17,
614 187–208, 2004.
- 615 Brasnett, B.: A global analysis of snow depth for numerical weather prediction. *J. Appl. Meteorol.* 38
616 (6), 726–740, 1999.
- 617 Brown, L.C., Howell, S.E., Mortin, J., Derksen, C.: Evaluation of the Interactive Multisensor Snow and
618 Ice Mapping System (IMS) for monitoring sea ice phenology. *Remote Sens. Environ.* 147,
619 65–78. doi: 10.1016/j.rse.2014.02.012, 2014.
- 620 Brown, R.D., Brasnett, B.: Canadian Meteorological Centre (CMC) Daily Snow Depth Analysis Data.
621 NASA National Snow and Ice Data Center Distributed Active Archive Center, Boulder,
622 Colorado, USA. <https://doi.org/10.5067/W9FOYWH0EQZ3>, 2010.
- 623 Brown, R.D., Brasnett, B., Robinson, D.: Gridded North American monthly snow depth and snow
624 water equivalent for GCM evaluation. *Atmos.–Ocean*, 41, 1–14, 2003.
- 625 Broxton, P.D., Zeng, X., Dawson, N.: The impact of a low bias in snow water equivalent initialization
626 on CFS seasonal forecasts. *J. Clim.* 30 (21), 8657–8671. [https://doi.org/10.1175/JCLI-D-17-](https://doi.org/10.1175/JCLI-D-17-0072.1)
627 0072.1, 2017.
- 628 Brubaker, K., Pinker, R., Deviatova, E.: Evaluation and comparison of MODIS and IMS snow-cover
629 estimates for the continental United States using station data. *J. Hydrometeorol.* 6, 1002–
630 1017, 2009.
- 631 Burke, E. J., Dankers, R., Jones, C. D., and Wiltshire, A. J.: A retrospective analysis of pan Arctic
632 permafrost using the JULES land surface model, *Clim. Dynam.*, 41, 1025–
633 1038, <https://doi.org/10.1007/s00382-012-1648-x>, 2013.
- 634 Chen, M., Wang, W., Kumar, A.: Prediction of monthly-mean temperature: The roles of atmospheric
635 and land initial conditions and sea surface temperature *J. Clim.* 23(3), 717–725, 2010.
- 636 Cho, E., Tuttle, S.E., Jacobs, J.M.: Evaluating consistency of snow water equivalent retrievals from
637 passive microwave sensors over the north central US: SSM/I vs. SSMIS and AMSR-E vs.
638 AMSR2. *Remote Sens.* 9(5), 465, 2017.
- 639 Cohen, J., Barlow, M., Kushner, P. J., Saito, K.: Stratosphere–troposphere coupling and links with
640 eurasian land surface variability. *J. Clim.* 20(21), 5335–5343.
641 <https://doi.org/10.1175/2007jcli1725.1>, 2007.

642 Collow, A.B.M., Thomas, N.P., Bosilovich, M.G., Lim, Y.K., Schubert, S.D., Koster, R.D.: Seasonal variability
643 in the mechanisms behind the 2020 Siberian heatwaves. *J. Clim.* 35(10), 3075–3090, 2022.

644 Dawson, N., Broxton, P., Zeng, X.: Evaluation of remotely sensed snow water equivalent and snow
645 cover extent over the contiguous United States. *J. Hydrometeorol.* 19 (11), 1777–1791.
646 <https://doi.org/10.1175/JHM-D-18-0007.1>, 2018.

647 De Angelis, A.M., Schubert, S.D., Chang, Y., Lim, Y.K., Koster, R.D., Wang, H., Marquardt Collow, A.B.:
648 Dynamical Drivers of the Exceptional Warmth over Siberia during the Spring of 2020. *J.*
649 *Clim.* 36(15), 4837–4861, 2023.

650 De Lannoy, G.J.M., Reichle, R.H., Houser, P.R., Arsenault, K.R., Verhoest, N.E.C., Pauwels, V.R.N.: Satellite-
651 scale snow water equivalent assimilation into a high-resolution land surface model. *J.*
652 *Hydrometeorol.* 11 (2), 352–369. <https://doi.org/10.1175/2009JHM1192.1>, 2010.

653 De Rosnay, P., Balsamo, G., Albergel, C., Muñoz-Sabater, J., Isaksen, L. Initialisation of land surface
654 variables for numerical weather prediction. *Surv. Geophys.* 35, 607–621, 2014.

655 Dee, D., Uppala, S., Simmons, A., Berrisford, P., Poli, P., Kobayashi, S., Andrae, U., Balsameda, M.,
656 Balsamo, G., Bauer, P., Bechtold, P., Beljaars, A.C.M., van de Berg, L., Bidlot, J., Bormann, N.,
657 Delsol, C., Dragani, R., Fuentes, M., Geer, A.J., Haimberger, L., Healy, S.B., Hersbach, H., Hólm,
658 E.V., Isaksen, L., Kållberg, P., Köhler, M., Matricardi, M., McNally, A.P., Monge-Sanz, B.M.,
659 Morcrette, J.-J., Park, B.-K., Peubey, C., de Rosnay, P., Tavolato, C., Thépaut, J.-N., Vitart, F.: The
660 ERA-Interim reanalysis: Configuration and performance of the data assimilation system. *Q.*
661 *J. R. Meteorol. Soc.* 137, 553–597, 2011.

662 Derome J, Lin H, Brunet, G.: Seasonal forecasting with a simple general circulation model: Predictive
663 skill in the AO and PNA. *J. Clim.*, 15, 597–609, 2005.

664 Dirmeyer, P.A.: The terrestrial segment of soil moisture–climate coupling. *Geophys. Res. Lett.* 38(16),
665 2011.

666 Dirmeyer, P.A., Gao, X., Zhao, M., Guo, Z., Oki, T., Hanasaki, N.: The Second Global Soil Wetness
667 Project (GSWP-2): Multi-model analysis and implications for our perception of the land
668 surface. *Bull. Amer. Meteor. Soc.* 87, 1381–1397, 2006.

669 Dutra, E., Schär, C., Viterbo, P., Miranda, P. M.: Land-atmosphere coupling associated with snow
670 cover. *Geophys. Res. Lett.* 38 (15) , 2011.

671 Dziubanski, D.J., Franz, K.J.: Assimilation of AMSR-E snow water equivalent data in a spatially-lumped
672 snow model. *J. Hydrol.* 540, 26–39. <https://doi.org/10.1016/j.jhydrol.2016.05.046>, 2016.

673 Essery, R.L.H., Rutter, N., Pomeroy, J., Baxter, R., Stahli, M., Gustafsson, D., Barr, A., Bartlett, P., Elder,
674 K.: SNOWMIP2: an evaluation of forest snow process simulations. *Bull. Amer. Meteor. Soc.*
675 90, 1120–1135, 2009.

676 Eagleson, P.S.: *Dynamic Hydrology*, McGraw-Hill, 1970

677 Foster, J.L., Sun, C., Walker, J.P., Kelly, R., Chang, A., Dong, J., Powell, H.: Quantifying the uncertainty
678 in passive microwave snow water equivalent observations. *Remote Sens. Environ.* 94, 187–
679 203, 2005.

680 Gan, Y., Zhang, Y., Kongoli, C., Grassotti, C., Liu, Y., Lee, Y. K., Seo, D. J.: Evaluation and blending of

681 ATMS and AMSR2 snow water equivalent retrievals over the conterminous United
682 States. *Remote Sens. Environ.* 254, 112280, 2021.

683 [Giroto, M., Musselman, K. N., and Essery, R. L. H.: Data Assimilation Improves Estimates of Climate-](#)
684 [Sensitive Seasonal Snow, Current Climate Change Reports, 6, 81–94,](#)
685 <https://doi.org/10.1007/s40641-020-00159-7>, 2020.

686 Gloege, L., Kornhuber, K., Skulovich, O., Pal, I., Zhou, S., Ciais, P., Gentine, P.: Land-Atmosphere Cascade
687 Fueled the 2020 Siberian Heatwave. *AGU Advances*, 3 (6), e2021AV000619, 2022.

688 Hamill, T.M., Whitaker, J.S., Snyder, C.: Distance-dependent filtering of background error covariance
689 estimates in an ensemble Kalman filter. *Mon. Weather Rev.* 129, 2776–2790, 2001.

690 Helfrich, S.R., McNamara, D., Ramsay, B.H., Baldwin, T., Kasheta, T.: Enhancements to, and forthcoming
691 developments in the interactive multisensor snow and ice mapping system (IMS). *Hydrol.*
692 *Process.* 21 (12), 1576–1586. <https://doi.org/10.1002/hyp.6720>, 2007.

693 Helmert, J., Şensoy Şorman, A., Montero, R.A., De Michele, C., De Rosnay, P., Dumont, M., Finger, D.,
694 Lange, M., Picard, G., Potopová, V., et al.: Review of Snow Data Assimilation Methods for
695 Hydrological, Land Surface, Meteorological and Climate Models: Results from a COST
696 HarmoSnow Survey. *Geoscience*, 8 (12), 489, 2018.

697 Houtekamer, P.L., Mitchell, H.L.: A sequential ensemble Kalman filter for atmospheric data
698 assimilation. *Mon. Weather Rev.* 129, 123–137, 2001.

699 Huning, L.S., AghaKouchak, A.: Global snow drought hot spots and characteristics. *Proc. Natl. Acad.*
700 *Sci.* 117(33), 19753-19759, 2020.

701 Hunt, B.R., Kostelich, E.J., Szunyogh, I.: Efficient data assimilation for spatiotemporal chaos: a local
702 ensemble transform Kalman filter. *Phys. D Nonlinear Phenom.* 230, 112–126, 2007.

703 Imaoka, K., Kachi, M., Kasahara, M., Ito, N., Nakagawa, K., Oki, T.: Instrument performance and
704 calibration of AMSR-E and AMSR2. *Int. Arch. Photogramm. Remote. Sens. Spat. Inf. Sci.* 38
705 (8), 13–16, 2010.

706 Jeong, J.H., Linderholm, H.W., Woo, S.H., Folland, C., Kim, B.M., Kim, S.J., Chen, D.: Impacts of snow
707 initialization on subseasonal forecasts of surface air temperature for the cold season. *J.*
708 *Clim.* 26 (6), 1956-1972, 2013.

709 Kobayashi, S., Ota, Y., Harada, Y., Ebata, A., Moriya, M., Onoda, H., Onogi, K., Kamahori, H., Kobayashi,
710 C., Endo, H.: The JRA-55 reanalysis: general specifications and basic characteristics. *J.*
711 *Meteorol. Soc. Jpn. Ser. II* 93, 5–48, 2015.

712 Koster, R.D., Dirmeyer, P.A., Guo, Z., Bonan, G., Chan, E., Cox, P., Gordon, C.T., Kanae, S., Kowalczyk,
713 E., Lawrence, D., Liu, P., Lu, C.H., Malyshev, S., McAvaney, B., Mitchell, K., Mocko, D., Oki,
714 T., Oleson, K., Pitman, A., Sud, Y.C., Taylor, C.M., Versegny, D., Vasic, R., Xue, Y., Yamada,
715 T., GLACE Team: Regions of strong coupling between soil moisture and
716 precipitation. *Science*, 305 (5687), 1138–
717 1140, <https://doi.org/10.1126/science.1100217>, 2004.

718 Koster, R.D., Mahanama, S., Yamada, T., Balsamo, G., Berg, A., Boisserie, M., Dirmeyer, P., Doblas-Reyes,
719 F., Drewitt, G., Gordon, C.: The second phase of the global land–atmosphere coupling

720 experiment: soil moisture contributions to subseasonal forecast skill. *J. Hydrometeorol.* 12,
721 805–822, 2011.

722 Kumar, S.V., Jasinski, M., Mocko, D.M., Rodell, M., Borak, J., Li, B., Beaudoin, H.K., Peters-Lidard, C.D.:
723 NCA-LDAS land analysis: development and performance of a multisensor, multivariate land
724 data assimilation system for the national climate assessment. *J. Hydrometeorol.* 20 (8), 1571–
725 1593. <https://doi.org/10.1175/JHM-D-17-0125.1>, 2019.

726 Kwon, Y., Yang, Z.-L., Hoar, T.J., Toure, A.M.: Improving the radiance assimilation performance in
727 estimating snow water storage across snow and land-cover types in North America. *J.*
728 *Hydrometeorol.* 18 (3), 651–668. <https://doi.org/10.1175/JHM-D-16-0102.1>, 2017.

729 [Lee, Y.K., Kongoli, C., Key, J.: An in-depth evaluation of heritage algorithms for snow cover and snow](#)
730 [depth using AMSR-E and AMSR2 measurements. *J. Atmos. Ocean. Technol.* 32\(12\), 2319-](#)
731 [2336, 2015.](#)

732 Li, F., Orsolini, Y.J., Keenlyside, N., Shen, M.L., Counillon, F., Wang, Y.G.: Impact of snow initialization
733 in subseasonal-to-seasonal winter forecasts with the Norwegian Climate Prediction
734 Model. *J. Geophys. Res. Atmos.* 124 (17-18), 10033-10048, 2019.

735 Li, F., Wang, H.: Autumn Eurasian snow depth, autumn Arctic sea ice cover and East Asian winter
736 monsoon. *Int. J. Climatol.* 34(13), 3616-3625, 2014.

737 Lim, S., Gim, H.J., Lee, E., Lee, S., Lee, W.Y., Lee, Y.H., Cassardo C., Park, S.K.: Optimization of snow-
738 related parameters in the Noah land surface model (v3. 4.1) using a micro-genetic algorithm
739 (v1. 7a). *Geosci. Model Dev.* 15(22), 8541-8559, 2022.

740 Liu, Y., Peters-Lidard, C.D., Kumar, S.V., Arsenault, K.R., Mocko, D.M.: Blending satellite-based snow
741 depth products with in situ observations for streamflow predictions in the upper Colorado
742 River basin. *Water Resour. Res.* 51 (2), 1182–1202. <https://doi.org/10.1002/2014WR016606>,
743 2015.

744 [Luoja, K., Pulliainen, J., Takala, M., Lemmetyinen, J., Mortimer, C., Derksen, C., Mudryk, L., Moisander,](#)
745 [M., Hiltunen, M., Smolander, T., Ikonen, J., Cohen, J., Salminen, M., Norberg, J., Veijola, K., and](#)
746 [Venäläinen, P.: GlobSnow v3.0 Northern Hemisphere snow water equivalent dataset, *Sci. Data,*](#)
747 [8, 163, <https://doi.org/10.1038/s41597-021-00939-2>, 2021.](#)

748 ~~Lee, Y.K., Kongoli, C., Key, J.: An in-depth evaluation of heritage algorithms for snow cover and snow~~
749 ~~depth using AMSR-E and AMSR2 measurements. *J. Atmos. Ocean. Technol.* 32(12), 2319-~~
750 ~~2336, 2015.~~

751 Meng, J., Yang, R., Wei, H., Ek, M., Gayno, G., Xie, P., Mitchell, K.: The land surface analysis in the
752 NCEP climate forecast system reanalysis. *J. Hydrometeorol.* doi:10.1175/JHM-D-11-090.1,
753 2012.

754 Meyal, A.Y., Versteeg, R., Alper, E., Johnson, D., Rodzianko, A., Franklin, M., Wainwright, H.: Automated
755 cloud based long short-term memory neural network based SWE prediction. *Front. Water*, 2,
756 574917, 2020.

757 Miyoshi, T., Yamane, S.: Local ensemble transform Kalman filtering with an AGCM at a T159/L48
758 resolution. *Mon. Weather Rev.* 135, 3841–3861, 2007.

759 [Oaida, C. M., Reager, J. T., Andreadis, K. M., David, C. H., Levoe, S. R., Painter, T. H., Bormann, K. J.,](#)
760 [Trangsrud, A. R., Giroto, M., and Famiglietti, J. S.: A High-Resolution Data Assimilation](#)
761 [Framework for Snow Water Equivalent Estimation across the Western United States and](#)
762 [Validation with the Airborne Snow Observatory, *J. Hydrometeorol.*, 20, 357–378,](#)
763 <https://doi.org/10.1175/JHM-D-18-0009.1>, 2019.

764 Orsolini, Y.J., Senan, R., Balsamo, G., Doblas-Reyes, F.J., Vitart, F., Weisheimer, A., Carrasco, A., Benestad,
765 R.E.: Impact of snow initialization on sub-seasonal forecasts. *Clim. Dyn.* 41, 1969–1982, 2013.

766 Orsolini, Y.J., Senan, R., Vitart, F., Weisheimer, A., Balsamo, G., Doblas-Reyes, F.: Influence of the
767 Eurasian snow on the negative North Atlantic Oscillation in subseasonal forecasts of the
768 cold winter 2009/10. *Clim. Dyn.* 47(3-4), 1325–1334. [https://doi.org/10.1007/s00382-015-](https://doi.org/10.1007/s00382-015-2903-8)
769 [2903-8](https://doi.org/10.1007/s00382-015-2903-8), 2016.

770 Overland, J. E., Wang, M.: The 2020 Siberian heat wave. *Int. J. Climatol.* 41, E2341–E2346, 2021.

771 Pullen, S., Jones, C., Rooney, G.: Using satellite-derived snow cover data to implement a snow analysis
772 in the met office NWP model. *J. Appl. Meteorol.* 50, 958–973. doi:10.1175/2010JAMC2527.1,
773 2011.

774 Pulliainen, J., Luojus, K., Derksen, C., Mudryk, L., Lemmetyinen, J., Salminen, M., Ikonen, J., Takala, M.,
775 Cohen, J., Smolander, T., Norberg, J.: Patterns and trends of Northern Hemisphere snow mass
776 from 1980 to 2018. *Nature*, 581 (7808), 294–298. [https://doi.org/10.1038/s41586-020-2258-](https://doi.org/10.1038/s41586-020-2258-0)
777 [0](https://doi.org/10.1038/s41586-020-2258-0), 2020.

778 Ramsay, B.H.: The interactive multisensor snow and ice mapping system. *Hydrol. Process.* 12 (10-11),
779 1537–1546, 1998.

780 Reichle, R.H.: Data assimilation methods in the Earth sciences. *Adv. Water Resour.* 31, 1411–1418,
781 2008.

782 Reichle, R.H., Draper, C.S., Liu, Q., Giroto, M., Mahanama, S.P., Koster, R.D., De Lannoy, G.J.:
783 Assessment of MERRA-2 land surface hydrology estimates. *J. Clim.* 30 (8), 2937–2960, 2017.

784 Reichle, R.H., Koster, R.D.: Bias reduction in short records of satellite soil moisture. *Geophys. Res. Lett.*
785 31, 2004.

786 Reichle, R.H., Koster, D., De Lannoy, G.J.M., Forman, B.A., Liu, Q., Mahanama, S.P.P., Toure, A.M.:
787 Assessment and Enhancement of MERRA Land Surface Hydrology Estimates. *J. Clim.* 24,
788 6322–6338, 2011.

789 Seo, E., Lee, M.I., Jeong, J.H., Koster, R.D., Schubert, S.D., Kim, H.M., Kim, D.H., Kang H.S., Kim, H.K.,
790 MacLachlan, C., Scaife, A.A.: Impact of soil moisture initialization on boreal summer
791 subseasonal forecasts: mid-latitude surface air temperature and heat wave
792 events. *Clim. Dyn.* 52, 1695–1709, 2019.

793 Seo, E., Lee, M.I., Reichle, R.H.: Assimilation of SMAP and ASCAT soil moisture retrievals into the
794 JULES land surface model using the Local Ensemble Transform Kalman Filter. *Remote Sens.*
795 *Environ.* 253, 112222, 2021.

796 Seo, E., Lee, M.I., Schubert, S.D., Koster, R.D., Kang, H.S.: Investigation of the 2016 Eurasia heat wave
797 as an event of the recent warming. *Environ. Res. Lett.* 15(11), 114018, 2020.

798 Shlyueva, A., Tolstykh, M., Mizyak, V., Rogutov, V.: Local ensemble transform Kalman filter data
799 assimilation system for the global semi-Lagrangian atmospheric model. *Russ. J. Numer. Anal.*
800 *Math. Model.* 28(4), 419-442, 2013.

801 [Smyth, E. J., Raleigh, M. S., and Small, E. E.: Improving SWE Estimation With Data Assimilation: The](#)
802 [Influence of Snow Depth Observation Timing and Uncertainty, *Water Resour. Res.*, 56,](#)
803 [e2019WR026853, <https://doi.org/10.1029/2019WR026853>, 2020.](#)

804 Sturm, M., Taras, B., Liston, G.E., Derksen, C., Jonas, T., Lea, J.: Estimating snow water equivalent using
805 snow depth data and climate classes. *J. Hydrometeor.* 11, 1380–1394, 2010.

806 Su, H., Yang, Z.-L., Dickinson, R.E., Wilson, C.R., Niu, G.-Y.: Multisensor snow data assimilation at the
807 continental scale: The value of gravity recovery and climate experiment terrestrial water
808 storage information. *J. Geophys. Res.*, 115, D10104, doi:10.1029/2009JD013035, 2010.

809 Takala, M., Luojus, K., Pulliainen, J., Derksen, C., Lemmetyinen, J., Karna, J.P., Koskinen, J., Bojkov, B.:
810 Estimating northern hemisphere snow water equivalent for climate research through
811 assimilation of space-borne radiometer data and ground-based measurements. *Remote*
812 *Sens. Environ.* 115:3517–3529, 2011.

813 Thomas, J.A., Berg, A.A., Merryfield, W.J.: Influence of snow and soil moisture initialization on sub-
814 seasonal predictability and forecast skill in boreal spring. *Clim. Dyn.* 47 (1), 49-65, 2016.

815 Toure, A.M., Luojus, K., Rodell, M., Beaudoin, H., Getirana, A.: Evaluation of simulated snow and
816 snowmelt timing in the Community Land Model using satellite-based products and
817 streamflow observations. *J. Adv. Model. Earth Syst.* 10(11), 2933-2951, 2018.

818 U.S. National Ice Center: IMS daily Northern Hemisphere snow and ice analysis at 1 km, 4 km, and
819 24 km resolutions, version 3. Boulder, Colorado, USA. NSIDC: National Snow and Ice Data
820 Center, accessed: 18 Aug 2022, <https://doi.org/10.7265/N52R3PMC>, 2008.

821 You, Y., Huang, C., Gu, J., Li, H., Hao, X., Hou, J.: Assessing snow simulation performance of typical
822 combination schemes within Noah-MP in northern Xinjiang, China. *J. Hydrol.* 581, 124380,
823 2020.

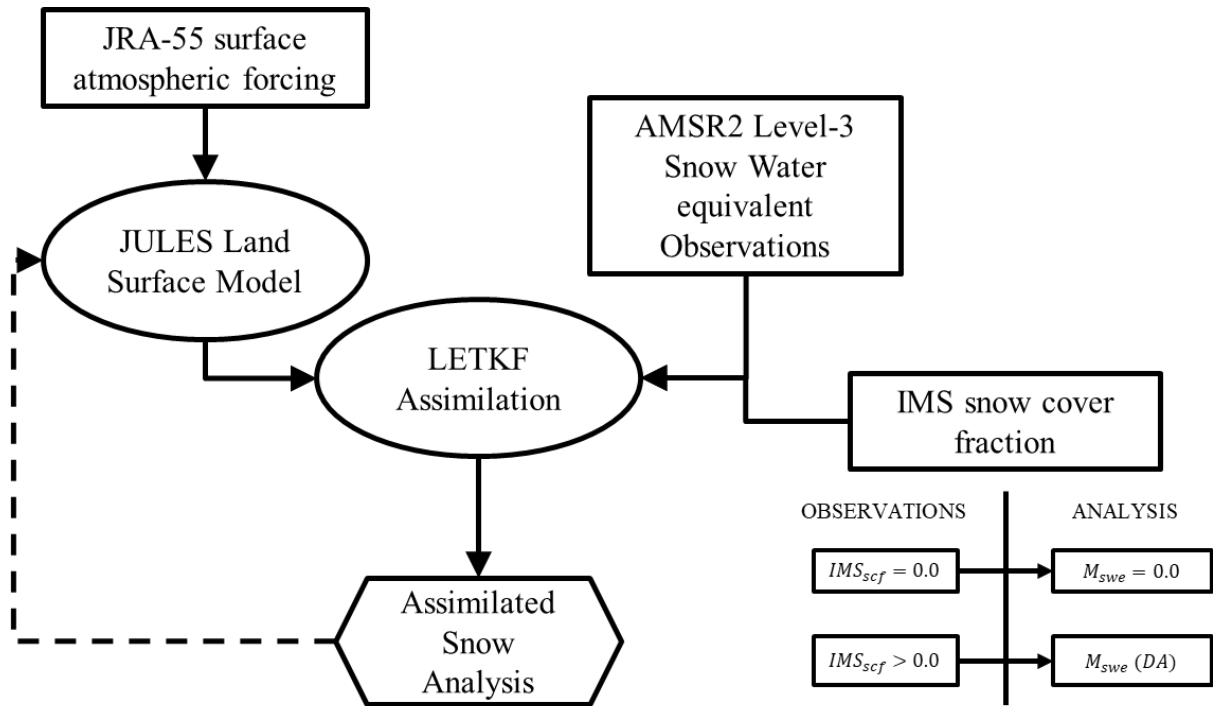
824

825 **Table 1.** Description of the land surface model, the data used, and assimilation experiment
 826 designs.

	INFORMATION	REFERENCES
Land Surface Model	JULES	Best et al., (2011)
Atmospheric Forcing	3-hourly JRA-55 reanalysis	Kobayashi et al., (2015)
Snow Observation	AMSR2 & IMS	Imaoka et al., (2010) Ramsay (1998) Helfrich et al., (2007)
Data Assimilation scheme	Local Ensemble Transform Kalman Filter (LETKF)	Hunt et al., (2007) Miyoshi and Yamane, (2007)
Resolution (km)	0.5° × 0.5° (~ 50)	
	1-day DA cycle	
Localization patch size (km)	3×3 (150), $\sigma = 30$	
Ensemble sizes	24	
Experiment period	2013-2020, APR	

827

828



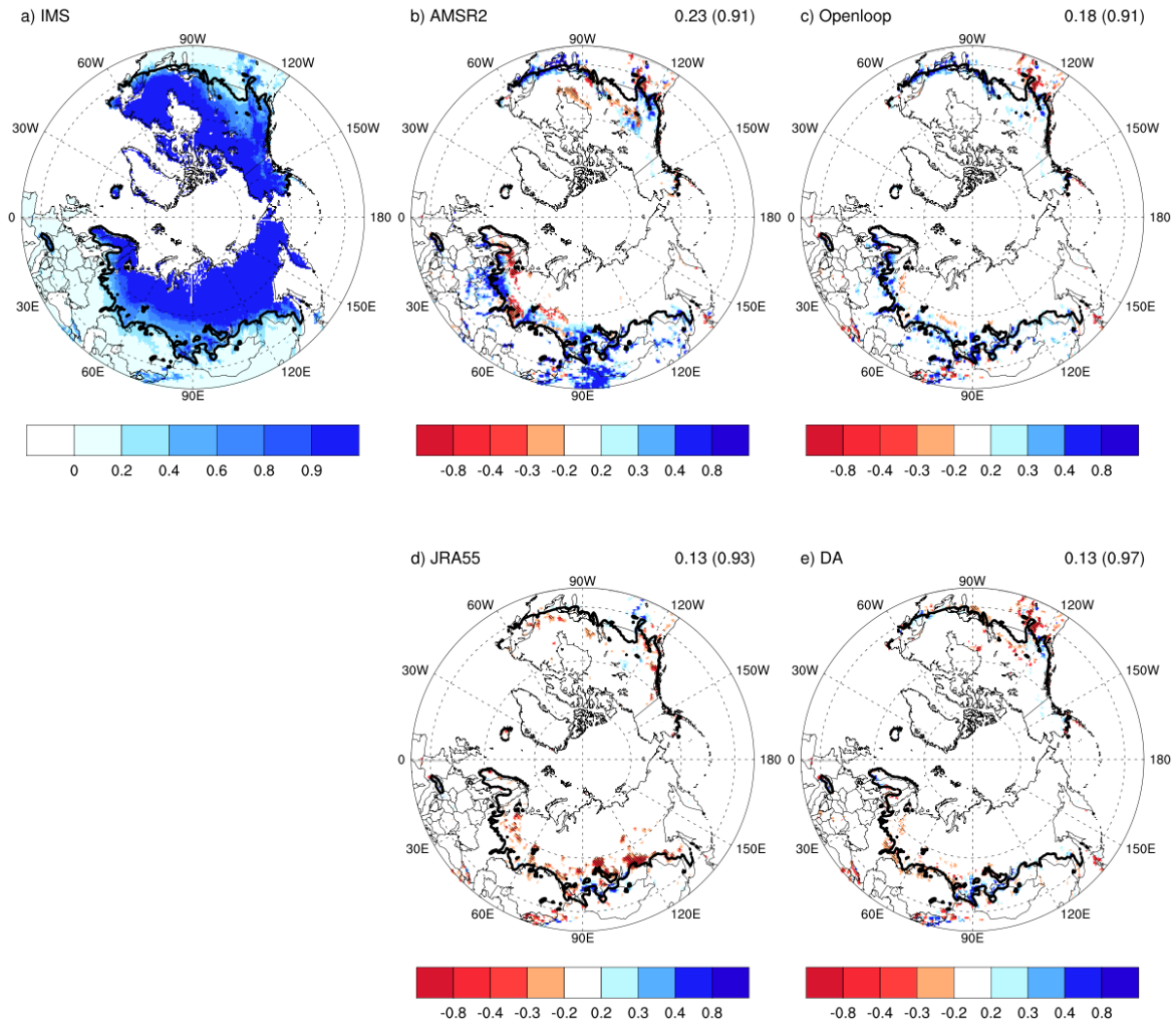
829

830 **Figure 1.** Schematic diagram of the snow assimilation system with satellite-derived

831 observations and the land surface model outputs.

832

833

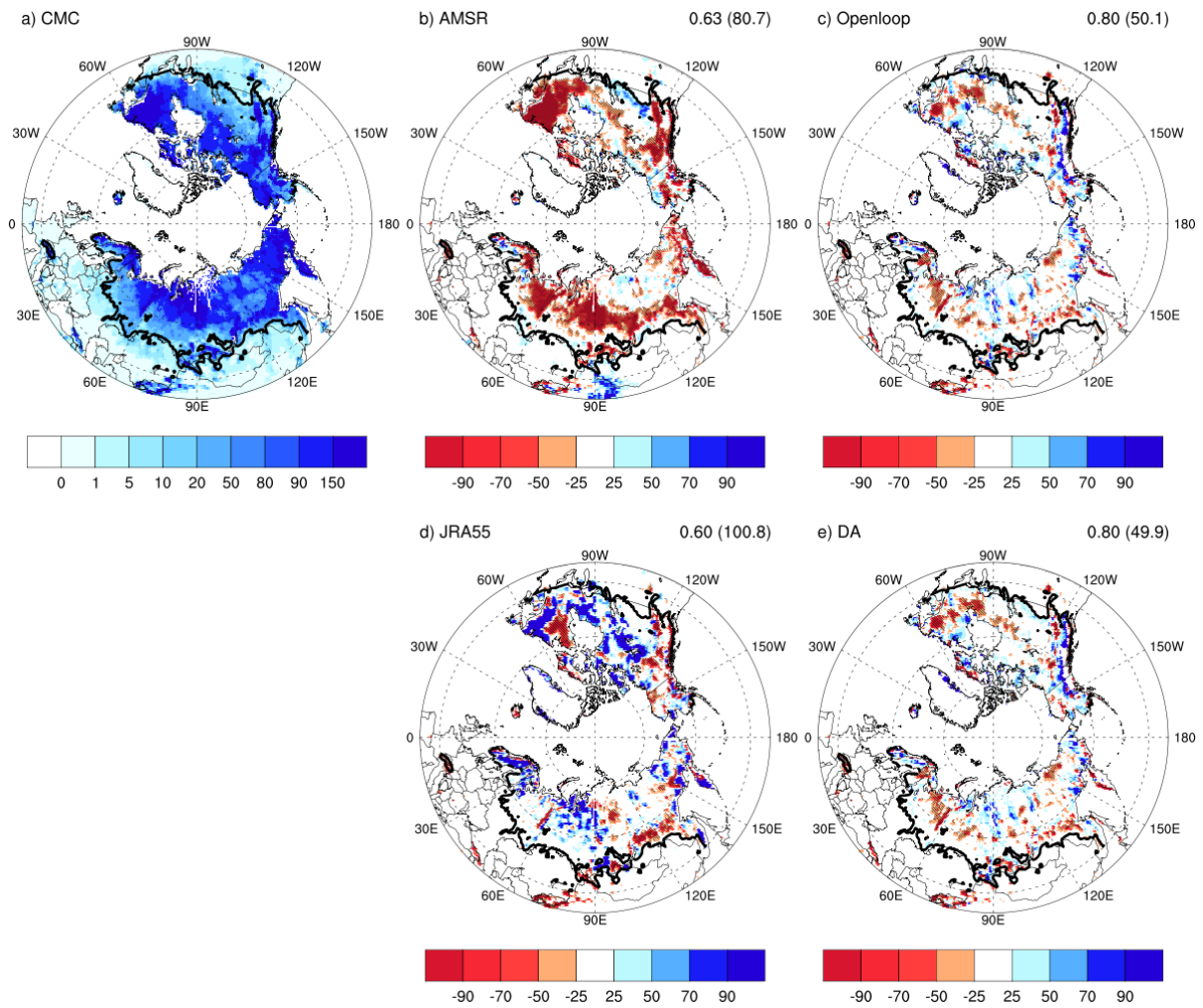


834

835 **Figure 2.** (a) Climatology of SCF from IMS used as reference and (b-e) the differences from
 836 IMS for AMSR2, base-line model simulation (Openloop), JRA55, and the data
 837 assimilation results (DA) for April during 2013-2020. The black line represents the
 838 boundary of the transition region, defined as the climatological-mean SWE of less than
 839 16mm. Each value on the top right is the root-mean-squared difference with IMS and
 840 the accuracy from IMS (parenthesis) for 15323 pixels over 40-60°N. The accuracy is
 841 defined in supplementary Table 1 as in previous study (Lee et al., 2015). Negative
 842 values in red shades are indicated with a diagonal line.

843

844

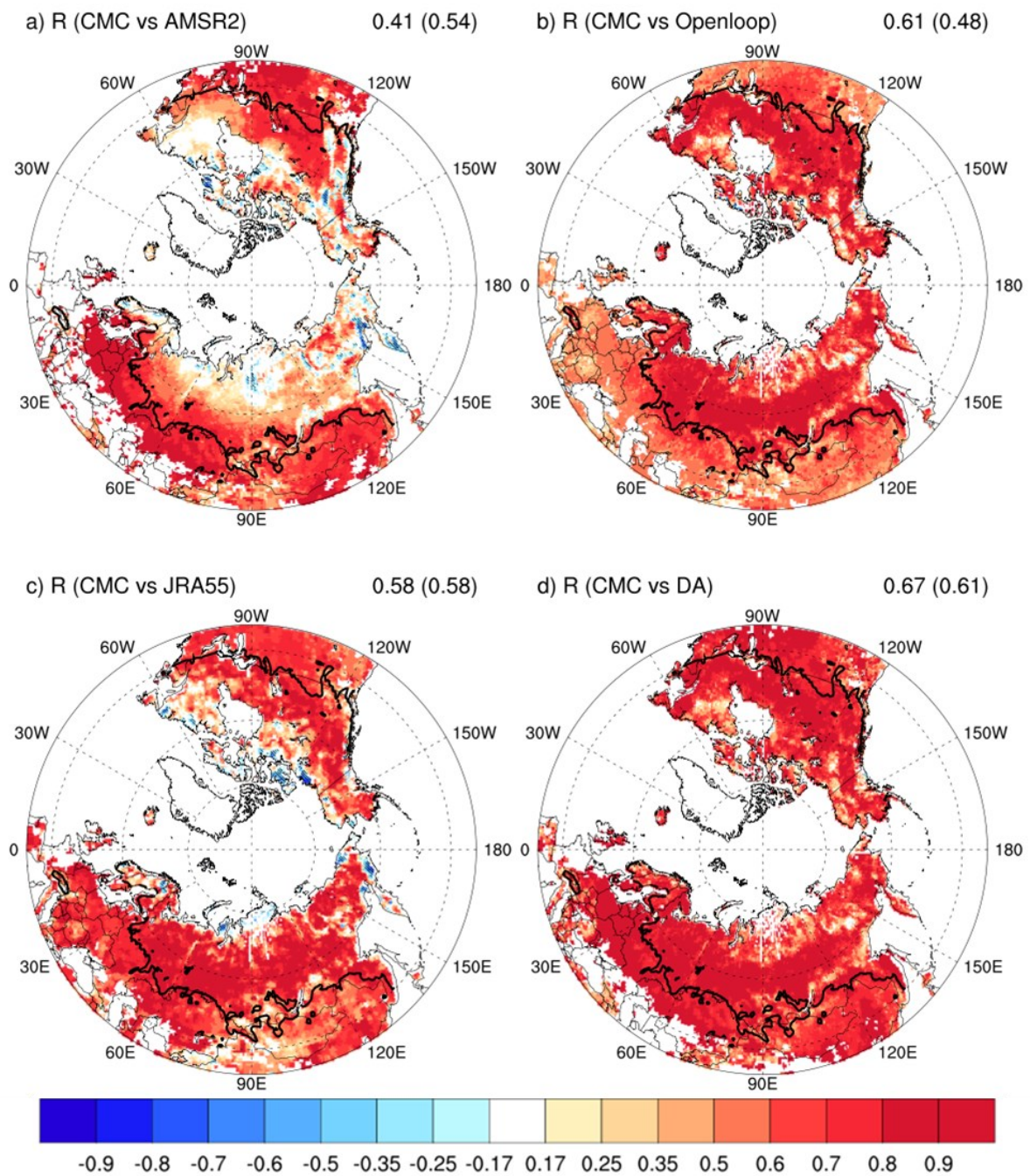


845

846 **Figure 3.** (a) Climatology of SWE from CMC used as reference and (b-e) the differences from
 847 CMC for AMSR2, base-line model simulation (Openloop), JRA55, and the data
 848 assimilation results (DA) for April during 2013-2020. The black line represents the
 849 boundary of the transition region, defined as the climatological-mean SWE of less than
 850 16mm. Each value on the top right is the pattern correlation with CMC for 26482 pixels
 851 over 40 °N and the root-mean-squared difference (unit: kg/m²) from CMC (parenthesis)
 852 for 15323 pixels over 40-60°N. Negative values in red shades are indicated with a
 853 diagonal line.

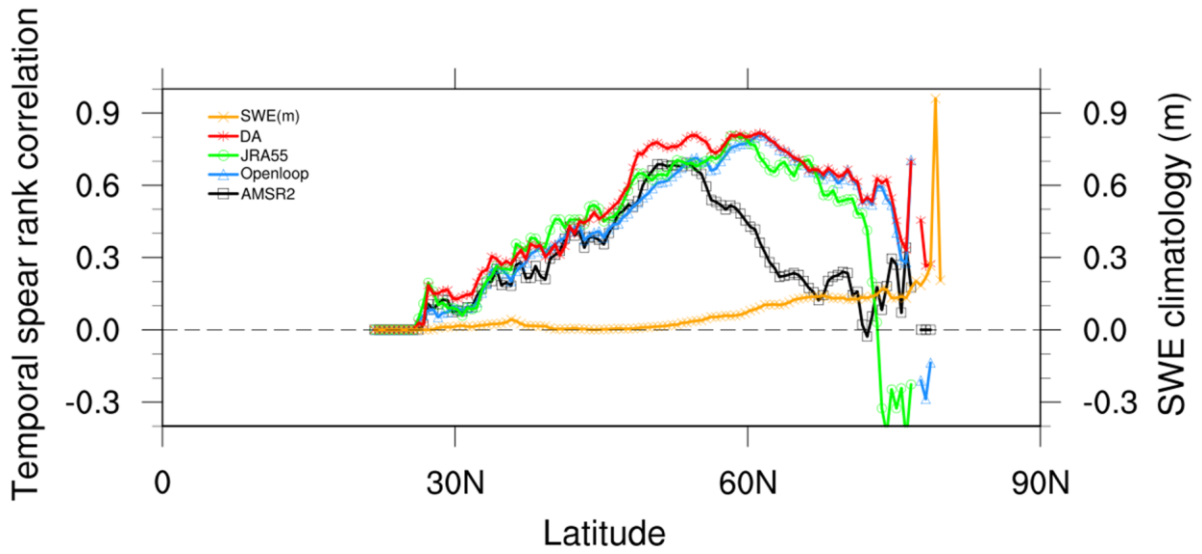
854

855



856

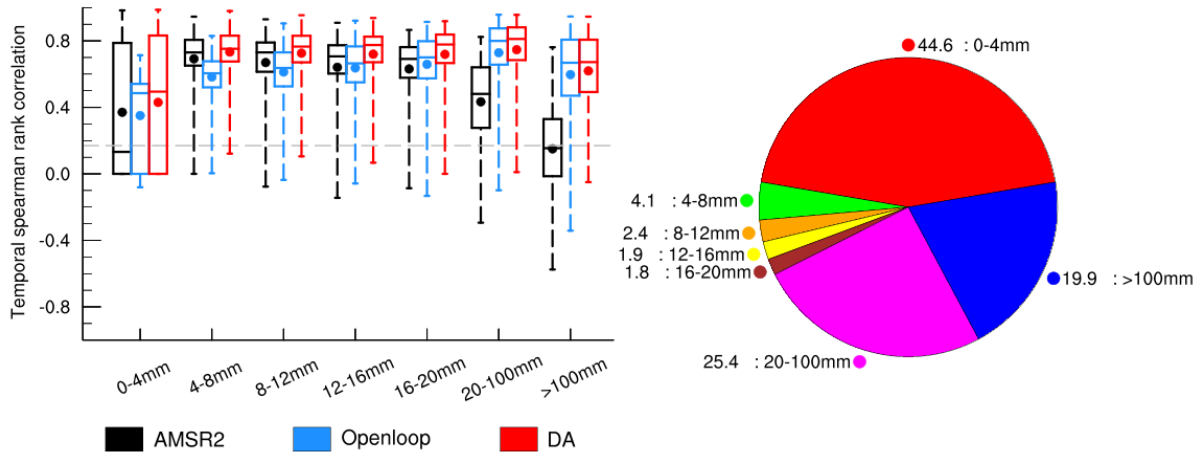
857 **Figure 4.** SWE skill measured as the Spearman rank correlation (R) with the CMC for AMSR2,
 858 base-line model simulation (Openloop), JRA55, and the data assimilation result (DA).
 859 The black line represents the boundary of the transition region, defined as the
 860 climatological-mean SWE of less than 16mm. Each value on the top is the area-average
 861 R of North hemisphere for 26482 pixels over 40°N and for 8801 pixels over the
 862 transition region (parenthesis). Negative values are indicated with a diagonal line.



863

864 **Figure 5.** Zonally-averaged Spearman rank correlation (R) along the latitude for SWE. The
 865 yellow line indicates the climatology of SWE, and the black, blue, green, and red lines
 866 denote the values of AMSR2, base-line model simulation (Openloop), JRA55, data
 867 assimilation results (DA), respectively.

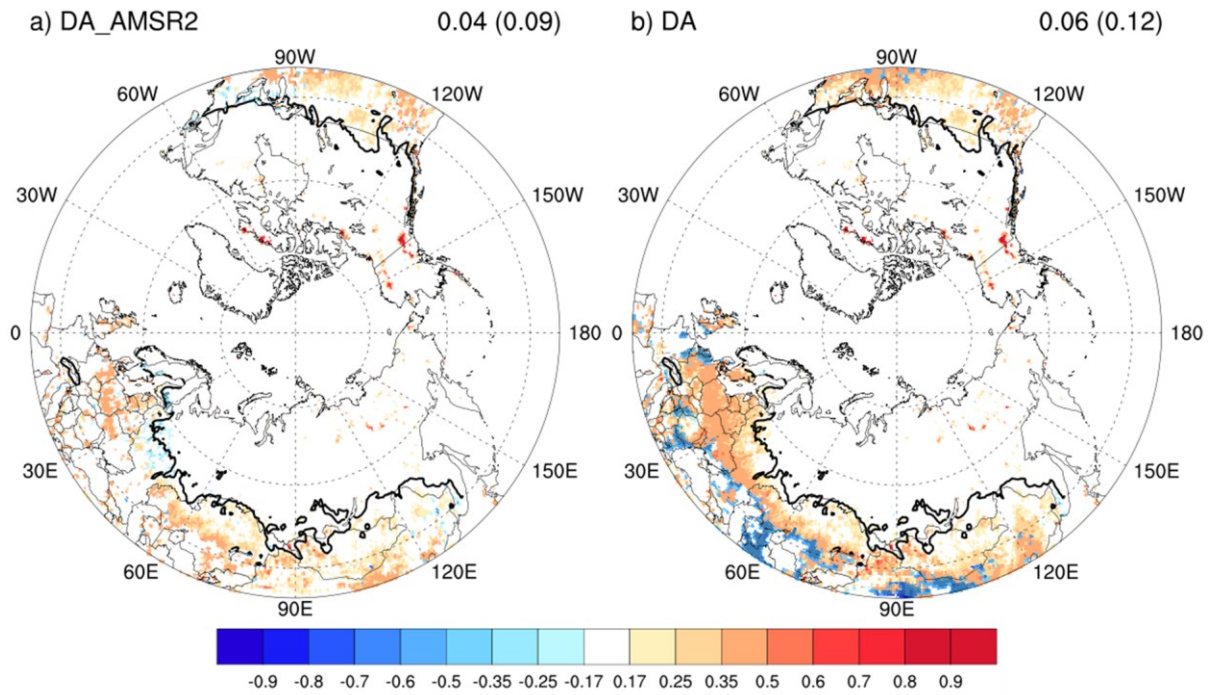
868



869

870 **Figure 6.** Box plots of the Spearman rank correlation (R) according to SWE. The pie chart
 871 shows the total area ratio (%) as a function of SWE amount. The black, blue, and red
 872 boxes denote the AMSR2, base-line model simulation (Openloop), and the data
 873 assimilation results (DA), respectively. The boxes indicate 25 and 75% percentiles, and
 874 the line and point in the boxes shows the median and the mean values. The upper and
 875 lower whiskers denote the 10 and 90% percentiles, respectively.

876



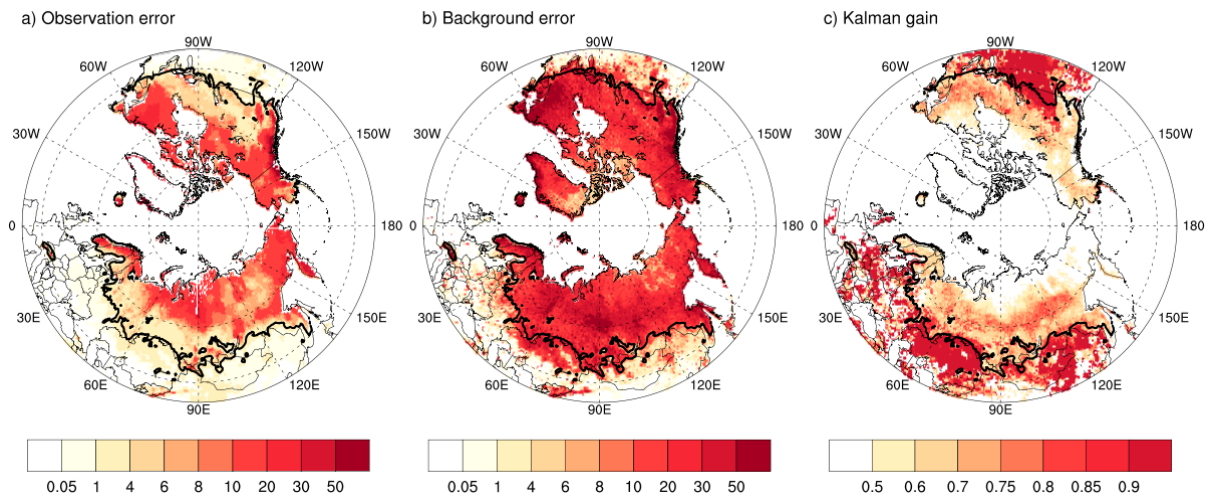
877

878 **Figure 7.** The difference in SWE Spearman rank correlation coefficient with CMC between
 879 the Openloop and data assimilation results: DA employing both AMSR2 and IMS and
 880 DA_AMSR2 utilizing solely AMSR2 and excluding IMS, for April during 2013-2020.
 881 The black line represents the boundary of the transition region, defined as the
 882 climatological-mean SWE of less than 16mm. Each value on the top right is the area-
 883 average over 40°N and the transition region (parenthesis). Negative values are indicated
 884 with a diagonal line.

885

886

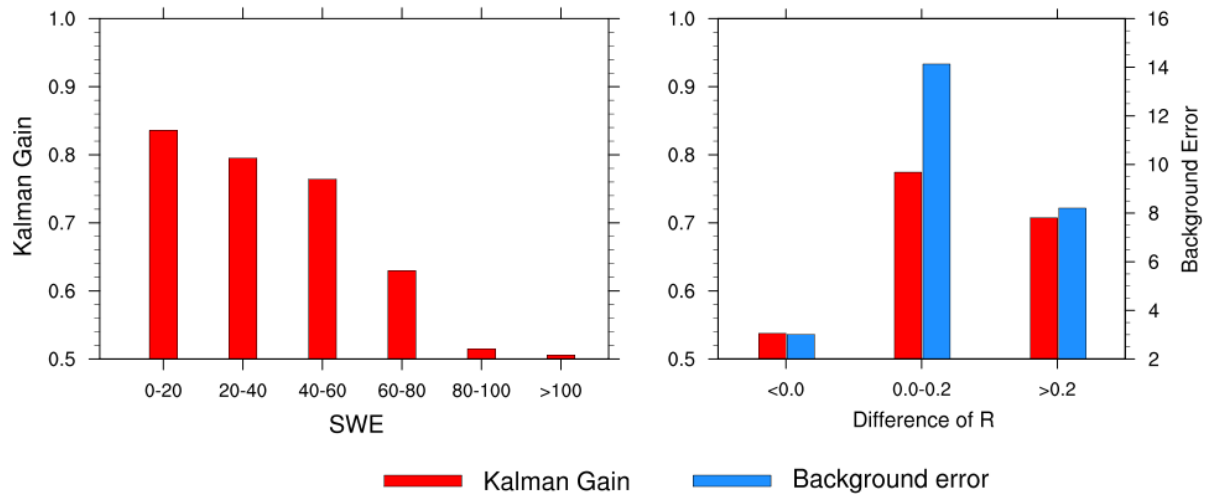
887



888

889 **Figure 8.** Spatial distribution of observation error (unit: kg/m^2), background error (unit: kg/m^2),
 890 and Kalman gain. The black line represents the boundary of the transition region,
 891 defined as the climatological-mean SWE of less than 16mm.

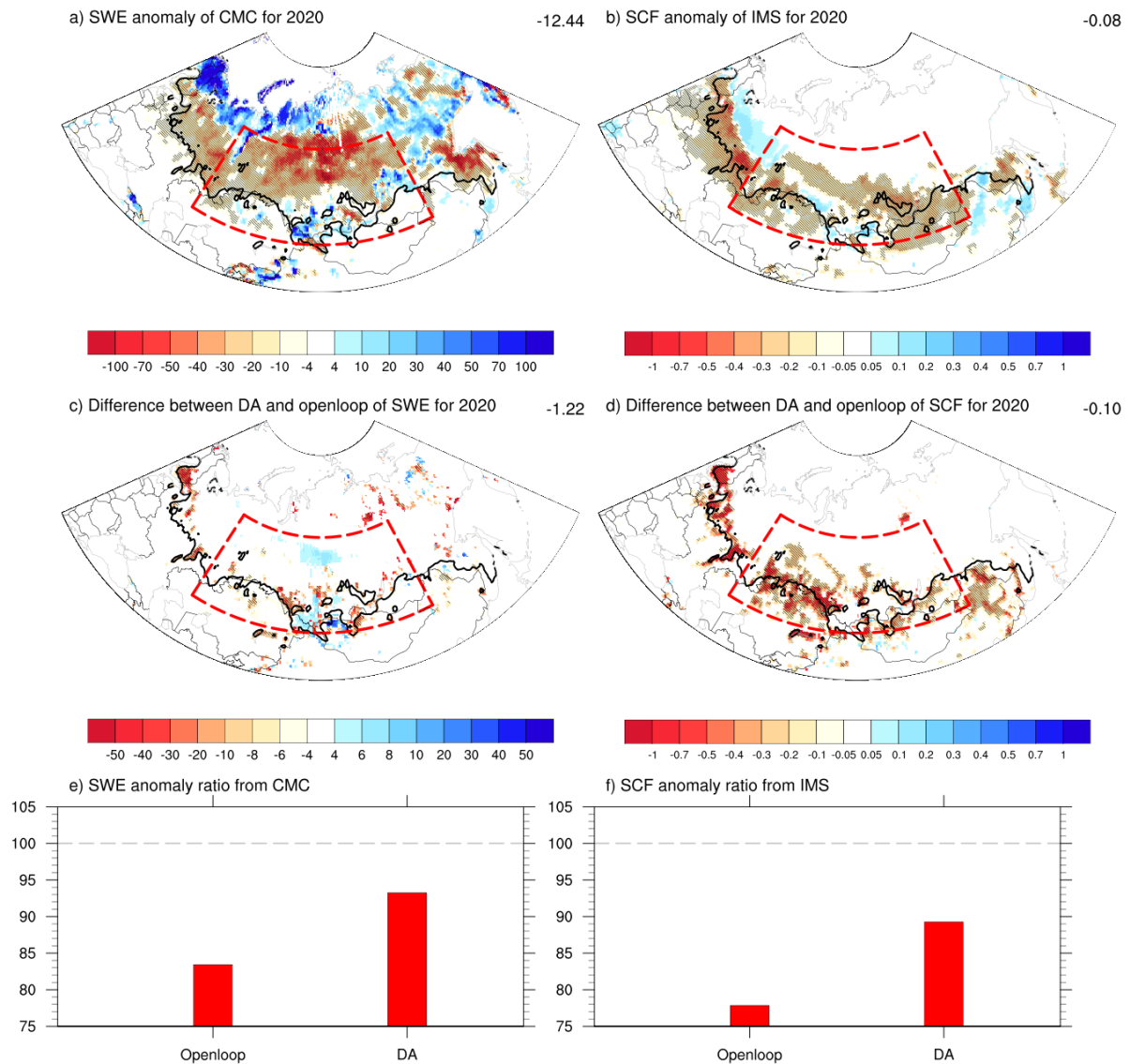
892



893

894 **Figure 9.** Bar chart of (left) the Kalman gain according to the SWE amount, and (right) the
 895 Kalman gain (red line) and background error (blue line) as a function of the difference
 896 between Openloop and DA in Spearman rank correlation coefficient (R).

897



898

899 **Figure 10.** Anomalies of a) SWE from CMC and b) SCF from IMS as well as the difference
 900 (c, d) of variables between DA and openloop in April 2020. Bar chart (e, f) indicates
 901 the ratio of DA and openloop to verification data such as CMC and IMS in the red box
 902 (48–65°N and 55–120°E), which is the region associated with extreme high-temperature
 903 events, focused on this study. Negative values are indicated with a diagonal line.

904

905